A Theoretical and Experimental Analysis of Radiofrequency Ablation with a Multielectrode, Phased, Duty-Cycled System

MICHAEL LAU, M.ENG.,* BETTY HU, M.S.,* RANDY WERNETH, M.S.,* MARSHALL SHERMAN, B.S.E.E.,* HAKAN ORAL, M.D.,† FRED MORADY, M.D.,† and PETR KRYSL, PH.D.‡

From the *Medtronic Ablation Frontiers, Carlsbad, California; †University of Michigan Health System, Ann Arbor, Michigan; and ‡University of California, San Diego, California

Background: *The development of a unique radiofrequency (RF) cardiac ablation system, for the treatment of cardiac arrhythmias, is driven by the clinical need to safely create large uniform lesions while controlling lesion depth. Computational analysis of a finite element model of a three-dimensional, multielectrode, cardiac ablation catheter, powered by a temperature-controlled, multiphase, duty-cycled RF generator, is presented.*

Methods: *The computational model for each of the five operating modes offered by the generator is compared to independent tissue temperature measurements taken during in vitro ablation experiments performed on bovine myocardium.*

Results: *The results of the model agree with experimental temperature measurements very closely—the average values for mean error, root mean square difference, and correlation coefficient were 1.9°C, 13.3%, and 0.97, respectively. Lesions are shown to be contiguous and no significant edge effects are observed.*

Conclusions: *Both the in vitro and computational model results demonstrate that lesion depth decreases consistently as the bipolar-to-unipolar ratio increases—suggesting a clinical application to potentially control lesion depth with higher fidelity than is currently available. The effect of variable design parameters and clinical conditions on RF ablation can now be expeditiously studied with this validated model. (PACE 2010; 33:1089–1100)*

ablation, multielectrode, radiofrequency, phasing, duty-cycle, finite element

Introduction

Radiofrequency (RF) catheter ablation is an accepted therapeutic approach for treating various types of cardiac arrhythmias such as supraventricular tachycardia, the Wolff–Parkinson–White Syndrome, atrial flutter, atrial fibrillation, and ventricular tachycardia.[1–3] Recently, a cardiac ablation system, consisting of a multielectrode ablation catheter driven by a phased, temperature-controlled, duty-cycled RF generator, has been developed. Initial reports using this system for pulmonary vein isolation during treatment of paroxysmal AF suggest significant reduction in both procedure and fluoroscopy times.[4]

A number of pioneering publications on the computational modeling of RF energy application have become available in the past 15 years and an excellent comprehensive review has recently appeared.[5] Computational modeling enables the study and optimization of design variables, such as electrode material/size/spacing/shape, and ablation parameters (energy delivery mode, target temperature, ablation duration, power control, power limit, etc.). *In vivo* and *in vitro* experimentation require physical prototypes to be built, and can be costly and time-consuming, sometimes resulting in irreproducible or inconclusive findings. In this article, we improve on established simulation methods to model-phased RF ablation with a unique cardiac ablation system, and validate the model using data collected from controlled *in vitro* ablation. The resulting model can be used in future work for design optimization and can be modified to model a variety of clinical conditions for further assessment of the performance of the ablation system.

Materials and Methods

RF Generator and Multi Array Ablation Catheter

The GENius™ Multi-Channel RF Ablation Generator (Medtronic Ablation Frontiers, Carlsbad, CA, USA) is a temperature-controlled, power-limited, multiphase system to deliver RF energy to multielectrode ablation catheters. Power output to each electrode is regulated to achieve and maintain an operator-defined target

Address for reprints: Michael Lau, M.Eng., 2210 Faraday Ave. Suite 100, Carlsbad, CA 92008. Fax: 760-827-0131; e-mail: michael.t.lau@medtronic.com

Received October 21, 2009; revised March 10, 2010; accepted March 29, 2010.

doi: 10.1111/j.1540-8159.2010.02801.x

temperature at the electrode–tissue interface (max power ranging from 6 to 10 W per electrode depending on energy mode). Through a combination of phasing and duty-cycling, the GENius RF Generator offers a selection of five operational modes, which control the ratio of bipolar-to-unipolar energy to be delivered: unipolar only, 1:1, 2:1, 4:1, or bipolar only. For example, the 4:1 energy mode indicates that 80% of the energy delivered is bipolar and the remaining 20% is unipolar. Clinically, 1:1 and 4:1 energy modes are the most widely used.

The Multi Array Ablation Catheter (MAAC™, Medtronic Ablation Frontiers) is composed of eight finned platinum electrodes capable of mapping and ablating in conjunction with the GENius RF Generator. Each 2-mm-long electrode is cylindrical at the tissue interface and with fins to increase convective cooling from blood flow, placating the need for active irrigation. The electrodes are affixed to an anatomically designed, X-shaped, collapsible nitinol frame (see Fig. 1A), intended to provide optimal contact across all electrodes, allowing for large area mapping and ablation of complex fractionated atrial electrograms. Each arm of the X-frame supports a pair of electrodes; with four pairs in total, each ablation is capable of creating up to four lesions. Each electrode has a thermocouple located directly at electrode–tissue interface for accurate independent temperature control. In clinical usage, recommended settings are 60°C target temperature and 60-second duration.

Experimental Methods

An *in vitro* ablation experimental setup, previously described,[6] was modified for this study to provide data for development and validation of the computational model. Briefly, a circulation

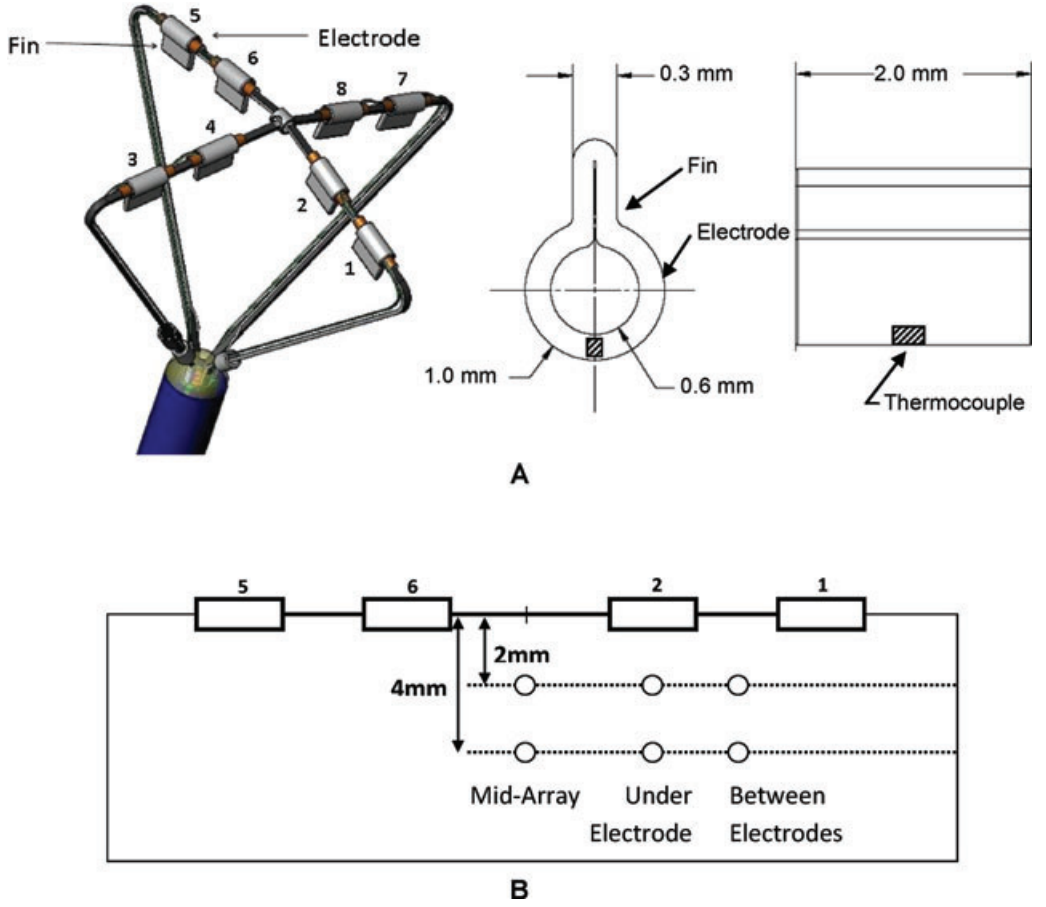

Figure 1. *(A) The Multi Array Ablation Catheter (MAAC) device. Each electrode contains a thermocouple and is driven by a separate PI controller. Electrode fins increase cooling, enabling more efficient energy delivery. Shaded areas show approximate location of thermocouple (not to scale). (B) A diagram of thermocouple placement at six locations within the tissue specimen for measuring experimental tissue temperature.*

system was set up to carry out *in vitro* ablation on bovine myocardium. A 16-L saline bath is attached to a precision inline heater (Infinity, Norwich, CT, USA), which maintained 0.5% saline at 37 ± 1°C. The 0.5% saline was delivered via a tube with an inner diameter (ID) of 12.7 mm attached to a swivel nozzle with 20 circular orifices with an ID of 1.85 mm to simulate local blood flow. The flow rate was adjusted to 1.8 L/min or 4.0 L/min using a flow meter (Cole Parmer, Vernon Hills, IL, USA). A force gauge (Imada, Northbrook, IL, USA) was mounted onto the x-y-z metric axis movement (Edmund Optics, Barrington, NJ, USA) to allow precise positioning of the catheter and consistent electrode–tissue contact.

Tissue specimens were obtained from fresh bovine hearts (Tip Top Meats, Carlsbad, CA, USA). A block of myocardial tissue (approximately 32 × 45 × 15 mm) was placed in an acrylic chamber with a ground plate. Tissue temperatures were recorded by T-type thermocouples (0.064-mm diameter with Teflon; time constant of 0.1 second; measurement accuracy of ±0.1°C; Physitemp, Clifton, NJ, USA). The thermocouples were placed at depths of 2 mm and 4 mm, in the following locations: underneath electrode 2, between electrodes 1 and 2, and under the mid array (see Fig. 1B). Ablations were conducted with a target temperature of 60°C for a 60-second duration at each energy mode (unipolar, 1:1, 2:1, 4:1, bipolar). At the conclusion of ablation, the blocks were dissected. Lesions were visually delineated as areas of marked tissue discoloration and measured from the surface of the tissue to the deepest point of the lesion using a metric scale under 10× magnification.

Bioheat Equation

As the experiments are performed *in vitro*, the bioheat equation may be simplified by neglecting metabolic heat generation and the heat exchange between tissue and blood (the perfusion effect). It is solved together with the Laplace equation for the rate of heat generation due to the resistive current

$$c_{pV}\dot{T} = \nabla \cdot (k\nabla T) + \sigma(T)\,\|\mathbf{E}\|^2, \quad \text{and}$$
$$\nabla \cdot (\sigma(T)\nabla\phi) = 0 \tag{1}$$

where T is the temperature, $\dot{T} = \frac{\partial T}{\partial t}$ is the rate of change in temperature, k is the thermal conductivity, c_{pV} is the specific heat per unit volume, $\mathbf{E} = -\nabla\phi$ is the electric field intensity expressed through the electric potential ϕ, and $\sigma(T)$ is the electrical conductivity as a function of temperature. In the present model, the material parameters k and c_{pV} are independent of the temperature, but if and when the temperature dependence becomes available for the materials at hand, the model will accommodate it. The two balance equations are coupled by the resistive heating term and the dependence of the electrical conductivity on the temperature, $\sigma(T)$. The quasi-stationary electrical equation is adequate for the RF of 500 kHz as the electrical impedance of tissue is mostly resistive at these frequencies.[7,8]

Geometry

The computational domain geometry was adopted in the form of a cylindrical subset of 16-mm radius of the rectangular tissue sample to reduce the computational effort. Two symmetry planes separating electrodes 1 and 2 from the rest have been adopted to further reduce the computational domain size. Thus the computational domain is the top quadrant in Figure 2A, shown as the computational mesh in Figure 2B. Note that the electrodes are pressed into the tissue by a small amount of force (corresponding to weight on the catheter of about 30 g), which means that as a reasonable first approximation we can consider the electrodes to be in the contact with the tissue through the bottom half of their entire circumference. Deformation of the tissue due to catheter placement is neglected. The electrical contact between the electrode and the tissue is assumed to be perfect, with no resistance to current flow passing from the ablation electrode to the tissue.

Thermal Boundary and Initial Conditions

The sample is immersed in a saline bath maintained at 37°C, which is taken as the initial temperature condition. The zero heat flux boundary condition was applied on the symmetry planes. On the bottom surface and on the side surfaces of the tissue block an artificial Newton's surface heat transfer term was applied as

$$q_n = h_a(T - T_b) \tag{2}$$

where q_n is the normal heat flux, T is the surface temperature, T_b is the temperature of the bath, and h_a is the artificial heat transfer coefficient whose value is chosen to approximate the heat flux from the sample into the surrounding environment, presumed to be at a constant temperature T_b. The numerical value was adopted, for numerical stability but otherwise arbitrarily, as $h_a = 5500\ \mathrm{W/(m^2 \cdot K)}$—varying this parameter by an order of magnitude affects the temperature at the sensors no more than 0.01°C.

On the top surface of the tissue block and the electrode surface (including the fin), exposed to the saline bath, a convective surface heat transfer term was applied to comprehensively account for the complex heat exchange between the sample and the flowing saline bath. This coefficient was

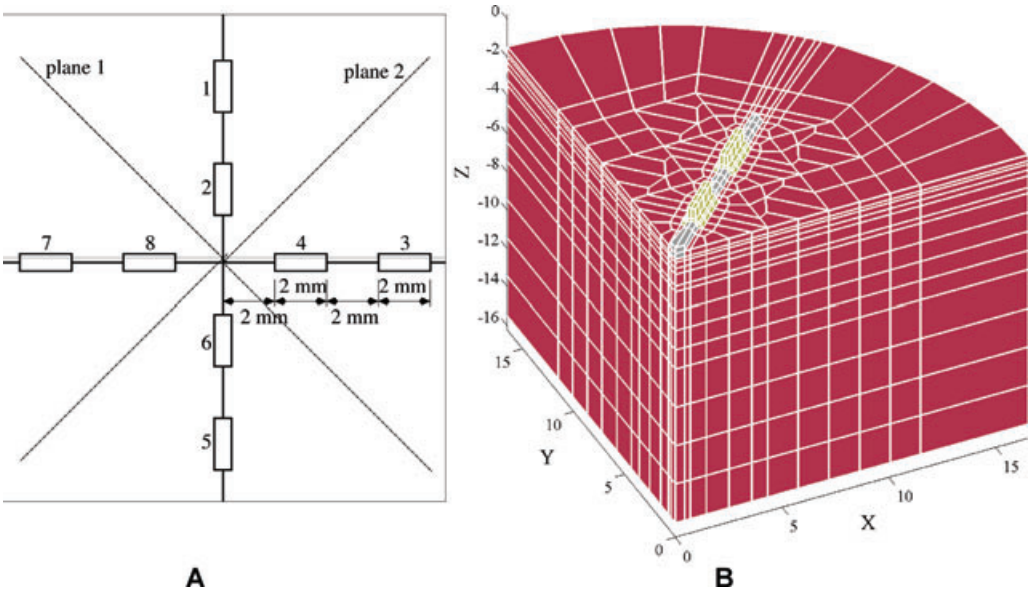

Figure 2. *(A) A schematic of the MAAC electrode orientation. During bipolar energy delivery, electrodes 1, 4, 6, and 7 are out of phase with electrodes 2, 3, 5, and 8. Plane 1 is a plane of symmetry and plane 2 is a plane of antisymmetry. (B) The computational mesh. Each cell represents either a quadratic 27-node element or a cubic 64-node element. Units of length, width, and depth as shown are millimeters.*

estimated from an *ad hoc* experiment described in the Appendix as $h_b = 2713$ W/(m$^2 \cdot$ K) and the numerical value agrees with analogous parameter values reported in the literature.[9–11]

Temperature Control and Electrical Boundary Conditions

Electrode temperature is measured by a thermocouple welded to the center of the electrode at the electrode–tissue interface. Power delivery to each electrode is controlled separately to achieve and maintain 60°C at each electrode during the ablation event. The control algorithm used in the generator hardware applies a fixed voltage waveform at near 500 kHz (phased depending on the selected energy mode) in duty cycles of only a few milliseconds, modulating the length of the "on" portion of the duty cycle to control power output. Replicating the hardware control exactly in the simulation would lead to significant associated computational cost and for this reason only an approximation to this control was implemented. In the simulation, unipolar and bipolar are assumed to each produce its own independent quasi-static potential field, with power output modulated by varying the voltage amplitude. The electrical problem is consequently solved twice in each time step, and the specific absorption rates are then mixed together in appropriate ratios for each of the five modes.

RF Generation of Heat

In unipolar energy delivery, for simplicity, the voltage of the dispersive electrode is fixed at a zero voltage, and the electrodes each have their own proportional-integral (PI) controller to apply the necessary voltage. The boundary condition prescribes the electric potential on the surface of the electrodes and on the bottom of the sample (the dispersive electrode). All other surfaces are associated with zero electric flux boundary condition. The parameters of the PI controllers of the two electrodes were taken as $K_p = 2.5$ V/K, $K_i = 0.0766$ V/(K $\cdot$ s), calibrated to approximate temperatures recorded at the electrodes for unipolar operation.

In bipolar energy delivery, the two electrodes of an electrode pair share a single PI controller to apply a voltage to electrode 1 and an opposite voltage to electrode 2. The hardware controller drives the electrodes so that the electrodes 1, 4, 6, and 7 are out of phase with electrodes 2, 3, 5, and 8. Consequently, plane 2 is a plane of asymmetry for the electrical problem (see Fig. 2A). The boundary condition prescribes the electric potential on the surface of the electrodes, zero electric flux through plane 1, and zero potential on plane 2. All other surfaces are associated with zero electric flux boundary condition. The parameters of the PI controller of the pair of active electrodes were taken as $K_p = 0.663$ V/K, $K_i = 0.021$ V/(K $\cdot$ s),

calibrated to approximate temperatures recorded at the electrodes for bipolar operation.

For the mixed-modes 1:1, 2:1, and 4:1 (bipolar-to-unipolar) energy modes, the electrical problem is solved twice in each time step, once for unipolar mode and once for bipolar mode. The electric field for each mode of heat generation is used to calculate the thermal load due to resistive heating, and the thermal loads are then mixed together in appropriate ratios.

Space Discretization

Figure 2B shows the isometric view of the 3,152 hexahedral cells that make up the computational domain. The mesh size is strongly graded from the largest elements (~5 mm) to the active electrodes (~0.3 mm) in order to capture the sharp gradients in both the electric and temperature fields. The same mesh is used for both the thermal and the electrical problem. The material properties used are given in Table I.

Each cell may be converted to either a quadratic (27-node) or a cubic (64-node) Lagrangean finite element. The difference between the results computed once with the quadratic discretization and once with the cubic discretization allows us to estimate the discretization error. The quadratic approximation leads to a total of approximately 55,000 coupled equations in the thermal-electrical computation; the cubic approximation results in a total of almost 180,000 coupled equations. The results obtained with the quadratic and the cubic discretization was a fraction of a degree Celsius; from this we conclude that the quadratic discretization was adequately accurate in space.

Time Discretization

The resulting ordinary differential equations that result from spatial discretization are

$$\mathbf{C}\dot{\mathbf{T}} + \mathbf{K}\mathbf{T} = \mathbf{L}(\mathbf{f}(\mathbf{T})), \quad \text{and} \quad \mathbf{A}(\mathbf{T})\mathbf{f} = \mathbf{b}(t) \tag{3}$$

where $\mathbf{T}$ and $\dot{\mathbf{T}}$ are vectors of nodal temperatures and rates of temperatures, $\mathbf{C}$ and $\mathbf{K}$ are the thermal capacity and conductivity matrix, $\mathbf{L}(\mathbf{f}(\mathbf{T}))$ is the thermal load, which incorporates the effect of the boundary conditions and the resistive heating as indicated by the vector of temperature-dependent nodal electric voltages $\mathbf{f}(\mathbf{T})$. $\mathbf{A}(\mathbf{T})$ is the temperature-dependent electrical conductivity matrix, and $\mathbf{b}(t)$ is the vector of time-dependent electrical loads. The coupled system is integrated in time using an adaptive implicit Euler method. The update formula from time t_0 to time t_1 results in a system of nonlinear algebraic equations for $\mathbf{T}_1, \mathbf{f}_1$

$$\big((\Delta t_1)^{-1}\mathbf{C} + \mathbf{K}\big)\mathbf{T}_1 = -(\Delta t_1)^{-1}\mathbf{C}\mathbf{T}_0 + \mathbf{L}(\mathbf{f}_1(\mathbf{T}_1)), \quad \text{and} \quad \mathbf{A}(\mathbf{T}_1)\mathbf{f}_1 = \mathbf{b}(t_1) \tag{4}$$

which is solved with fixed-point iteration to tolerance of 0.002°C as the maximum change in temperature between successive iterations. At difference with prior treatments, the time step is adjusted adaptively without user intervention using the formula

Table I.

List of Material Properties Used in the Computational Model

Symbol	Quantity	Value and Units
k_t	Thermal conductivity of bovine heart tissue	0.55×10^{-3} W/(mm · K)
ρ_t	Mass density of bovine heart tissue	1.2×10^{-6} kg · mm^{-3}
c_{pVt}	Specific heat per unit volume of bovine heart tissue	3200 ρ_t J/(mm^3 · K)
σ_t	Electric conductivity of bovine heart tissue	2.22×10^{-4} $(1 + 0.02(T - 37))$ S/mm
k_e	Thermal conductivity of platinum electrode	73×10^{-3} W/(mm · K)
ρ_e	Mass density of electrode	21.44×10^{-6} kg · mm^{-3}
c_{pVe}	Specific heat per unit volume of electrode	132.51 ρ_e J/(mm^3 · K)
σ_w	Electric conductivity of nitinol wire*	1.0×10^{-6} S/mm
k_w	Thermal conductivity of nitinol wire	18×10^{-3} W/(mm · K)
ρ_w	Mass density of nitinol wire	6.5×10^{-6} kg · mm^{-3}
c_{pVw}	Specific heat per unit volume of nitinol wire	322 ρ_w J/(mm^3 · K)

*In reality, the wires are electrically insulated, but in our study we achieve the same effect by artificially reducing the electrical conductivity of the nitinol wire to a very low value to avoid short-circuiting the wire to the electrodes.

$$\Delta t_1 = \Delta t_0 \sqrt{\frac{tol}{e_p}}, \quad \text{where}$$
$$e_p = \left\| \mathbf{T}_1 - \mathbf{T}_0 - \frac{\Delta t_0}{\Delta t_{-1}} (\mathbf{T}_0 - \mathbf{T}_{-1}) \right\|_\infty \quad (5)$$

Here Δt_1 and Δt_0 are the desired and the current time step, *tol* is a user-defined temperature tolerance (taken as 0.5°C here). Further, e_p is the predicted temperature error, which is an approximation of the second-order term of the Taylor series for the temperature. $\mathbf{T}_1$, $\mathbf{T}_0$, $\mathbf{T}_{-1}$ are the vectors of nodal temperatures at the end and at the beginning of the current and previous time steps.

Implementation

All computations have been implemented and performed using MATLAB (MathWorks, Natick, MA, USA) with the finite element toolkit SOFEA.[12] This allowed us to incorporate all computations in an integrated framework that executes without user intervention.

Model Accuracy Evaluation

To quantify the accuracy of the model, the predicted temperature from six locations in the heart tissue were compared to experiment results using the three indicators presented by Jain and Wolf: (a) the mean temperature error

$$\bar{T} = \frac{\int_0^\tau (T_m - T_e) d\tau}{t} \quad (6)$$

where t is ablation duration (60s), T_e is experimental temperature measurement (°C), and T_m is model temperature prediction (°C); (b) the rms difference

$$\text{Diff}_{\text{rms}} = \frac{\sqrt{\sum_{i=1}^{n} \frac{(T_{ei} - T_{mi})^2}{n}}}{T_{e60} - 37} \times 100\% \quad (7)$$

where T_{ei} is experimental temperature measurement at time i (°C), T_{mi} is model temperature at time i (°C), n is the number of time steps, and T_{e60} is experimental temperature at 60 seconds (°C); and (c) the correlation coefficient r.[10]

Results

Simulation and *in vitro* results were obtained at each location for each of the five energy delivery modes. For brevity, we only report tissue temperature results for the bipolar-to-unipolar modes used most widely in the clinical setting, 1:1 and 4:1. Figure 3 compares the measured *in vitro* tissue temperature to the computed temperatures over the duration of the 60 second ablation and the following 60 seconds after ablation for the (a) 1:1 energy mode and (b) 4:1 energy mode. Table II shows the model accuracy indicators, calculated for each location and each energy mode. Overall the model predicted tissue temperature very closely—the average values for mean error, root mean square difference, and correlation coefficient were 1.9°C, 13.3%, and 0.97, respectively.

Figure 4 depicts representative lesions for the (a) 1:1 and (b) 4:1 energy modes. Figure 5 compares the *in vitro* lesion measurements with the maximum depth attained by computational results according to: (a) the $T_{\text{Max}} \geq 60$°C boundary surface (tissue temperature reaching at least 60°C),[13] (b) the $T_{\text{Max}} \geq 50$°C boundary surface (tissue temperature reaching at least 50°C),[14] (c) the "cumulative equivalent minutes at 43°C" criterion (we assume CEM43 = 128 minutes to be representative of values considered for cardiac tissue[15]), and (d) the Arrhenius chemical reaction rate relationship ($\Omega = 1$ represents irreversible damage),[16] where the parameters are those reported in the open literature for swine and human skin.[8] The predicted $T_{\text{Max}} \geq 60$°C boundary closely agrees with the *in vitro* lesion measurement of tissue discoloration (as seen in Fig. 5A), while the $T_{\text{Max}} \geq 50$°C agrees with the other methods of predicting tissue viability (as seen in Fig. 5B–D). All computational predictions as well as the *in vitro* data show that as the percentage of unipolar power decreases, lesion depth decreases. The temperature distribution is illustrated in Figure 6, which shows isothermal surfaces for selected time intervals of RF heating for the (a) 1:1 energy mode and (b) 4:1 energy mode. Note that only half of the computational domain is shown to expose the interior of the domain. The shape and symmetry of the temperature profiles at 60 seconds qualitatively agree with the resulting *in vitro* lesions.

Discussion

The improvements made over previous simulation methods are incremental but nonetheless important. The most notable contributions are the integration of the device controller into simulation time steps, the control of simulation accuracy by varying high-order finite elements in space and adaptively in time, and the model for mixed power delivery for the several operating modes of the catheter. The results illustrate that the finite element model accurately reproduces the temperature distribution in the tissues as measured from *in vitro* experiments. In all cases, the computational model predicted tissue temperature well, though it was slightly more accurate at predicting temperatures for the mixed modes (1:1, 2:1, and

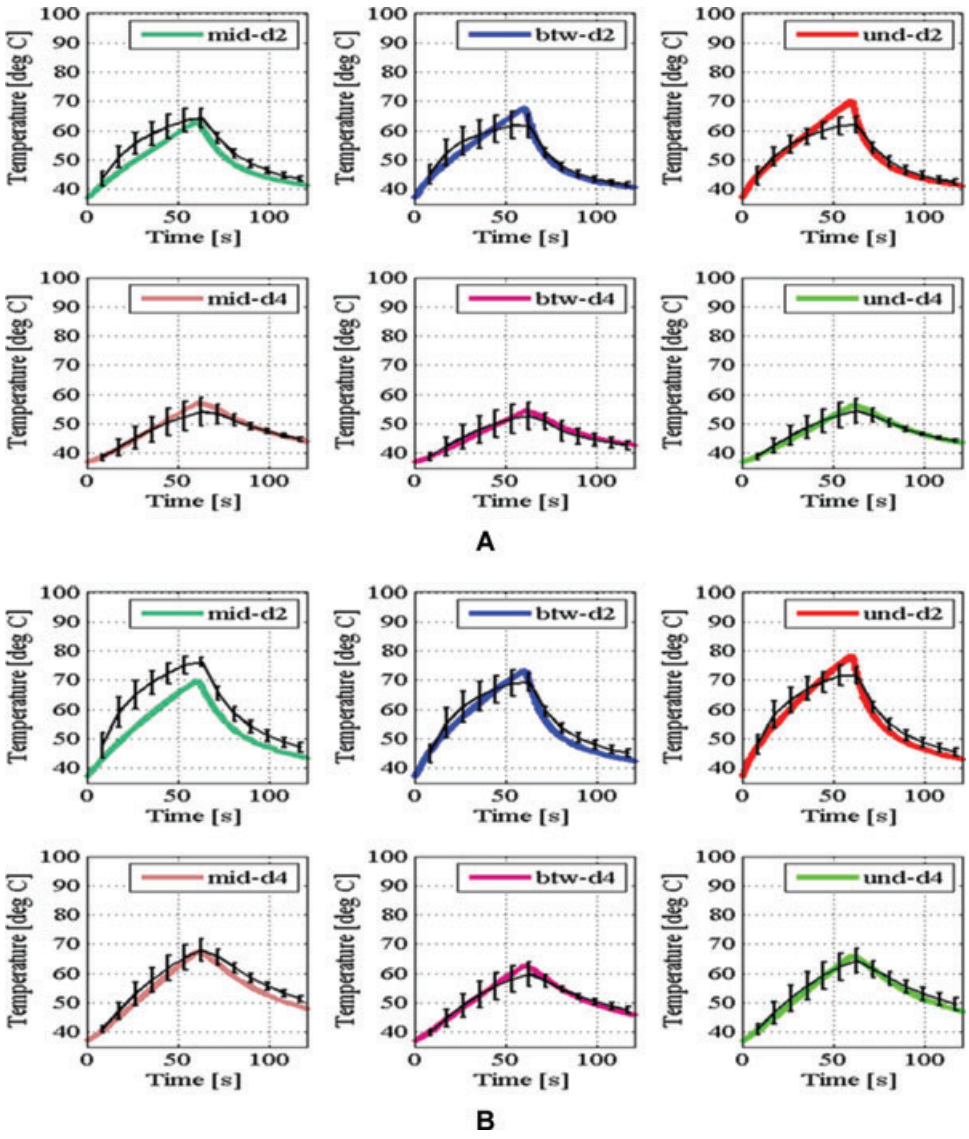

Figure 3. *(A) Tissue temperature results for 1:1 (bipolar-to-unipolar) energy mode. (B) Tissue temperature results for 4:1 (bipolar-to-unipolar) energy mode. In vitro temperatures in six locations: "und": under electrodes; "btw": between electrodes; "mid": mid-array; "d2": 2-mm depth; "d4": 4-mm depth. Error bars denote standard deviations from five RF applications. Computational model results are shown by the solid lines.*

4:1 energy modes), which include the two most widely used energy modes clinically, 1:1 and 4:1.

In Figure 3, the predicted temperature at the mid-array location (mid-d2) slightly underestimates the *in vitro* temperature results. We conjecture that this is due to error in the *in vitro* measurement, caused by conduction of heat from adjacent electrode pairs along the thermocouple wire leads toward the thermocouple gauge tip. There is also slight over-prediction of the tissue temperatures toward the end of the heating phase. Both the unipolar and the bipolar PI controller display slight temperature overshoot, which is not observed with the hardware controller. The difference is likely due to the continuous function of the controllers in the computational model, as opposed to the duty cycle of the hardware controller. The mismatch may also be partially due to the material properties being assumed independent of the temperature. Another limitation of the model is in the implementation of the power delivery. The model assumes independent unipolar and bipolar fields, which combine to create the thermal effect of the mixed modes. However, in

Table II.

Comparison of Experimental and Computational Results at Six Locations for Five Energy Modes Using the Three Indicators

	Unipolar			1:1			2:1			4:1			Bipolar		
	$\bar{T}$	Diff_{rms}	r	$\bar{T}$	Diff_{rms}	r	$\bar{T}$	Diff_{rms}	r	$\bar{T}$	Diff_{rms}	r	$\bar{T}$	Diff_{rms}	r
mid-2mm	3.7	9.8%	0.99	2.4	10.4%	0.97	1.1	6.9%	0.98	1.7	13.1%	0.93	3.6	19.0%	0.95
btw-2mm	7.5	17.9%	0.95	3.3	10.7%	0.98	1.8	11.5%	0.96	0.9	8.7%	0.98	1.6	16.7%	0.91
und-2mm	5.2	14.3%	0.93	3.5	11.1%	0.97	1.1	11.7%	0.95	1.0	10.3%	0.96	3.7	16.6%	0.97
mid-4mm	−4.1	19.2%	0.93	−2.9	16.2%	0.99	−2.5	16.8%	0.99	−1.9	17.2%	0.96	1.1	10.9%	0.99
btw-4mm	4.3	14.1%	0.97	2.7	10.6%	0.99	1.0	7.5%	0.98	1.1	7.2%	0.99	2.9	26.9%	0.97
und-4mm	5.8	14.5%	0.99	3.1	11.0%	0.99	0.5	6.5%	0.98	0.1	4.8%	0.99	3.6	27.4%	0.98
Average	3.7	15.0%	0.96	2.0	11.7%	0.98	0.5	10.1%	0.97	0.5	10.2%	0.97	2.8	19.6%	0.96

$\bar{T}$ = the mean temperature error (°C); Diff_{rms} = the rms difference; and r = the correlation coefficient.

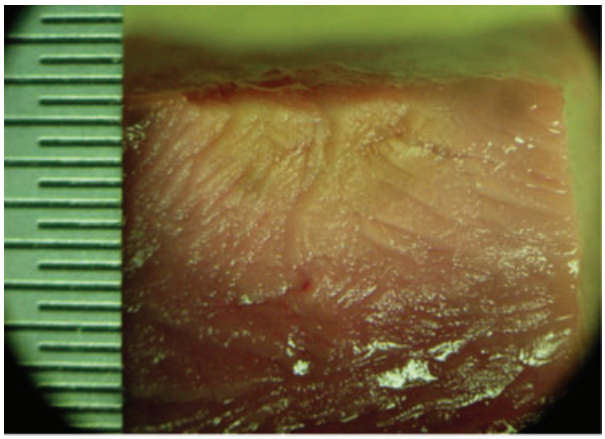

A

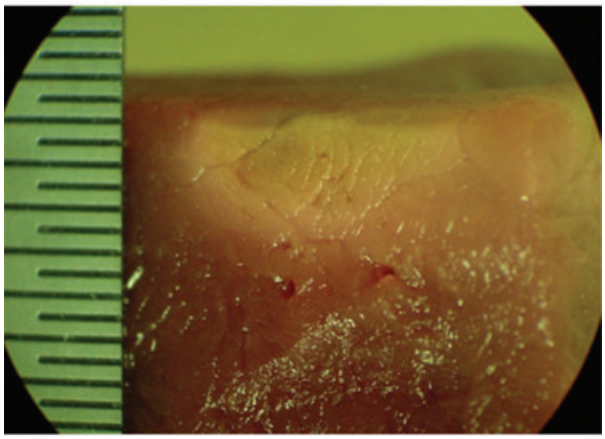

B

Figure 4. *Representative photographs of lesions created in vitro with the MAAC device (taken under 10× magnification). Ablations performed with a target temperature of 60°C for 60 seconds in the (A) 1:1 and (B) 4:1 (bipolar-to-unipolar) energy modes. Ruler increments at 0.5 mm.*

reality, the hardware delivers power through a combination of phasing and mixing duty-cycles to achieve the mixed modes. Despite these minor discrepancies and limitations, the computational model accurately predicts the temperature profile in the tissue as a function of time during ablations for the various energy modes.

Experimental data from *in vivo* ablations were not suitable for model comparison due to the wide variation in data as a result of limited sample size and the uncontrolled conditions of the *in vivo* environment. In addition, previous work has shown that the perfusion effect is negligible[17] and established *in vitro* experiments as a suitable proxy.[6] The large standard deviation in the measured *in vitro* tissue temperature is likely due to limitations of the experimental setup and variations between tissue samples. Tissue temperature data are measured from T-type thermocouples inserted into the tissue at specified locations; however, placing the thermocouples with high spatial accuracy is difficult. In addition, inconsistencies between tissue samples (fascia, fat content, surface texture, freshness) can cause differences in thermal conductivity and lesion discoloration, which may affect measurements. More importantly, firmness and elasticity of the tissue vary, resulting in inconsistent electrode contact surface area, affecting current density and electrode cooling. The difficulty in achieving reliable and reproducible data from *in vitro* and *in vivo* experiments substantiates the need for computational modeling.

Computational model results for lesion depth (see Fig. 5) are consistent with previous work by Panescu et al., which has shown that lesion discoloration (as measured *in vitro*) is well matched by tissue temperature of 60°C whereas lesion depth according to tissue viability is well matched by tissue temperature of 50°C.[13] Zheng

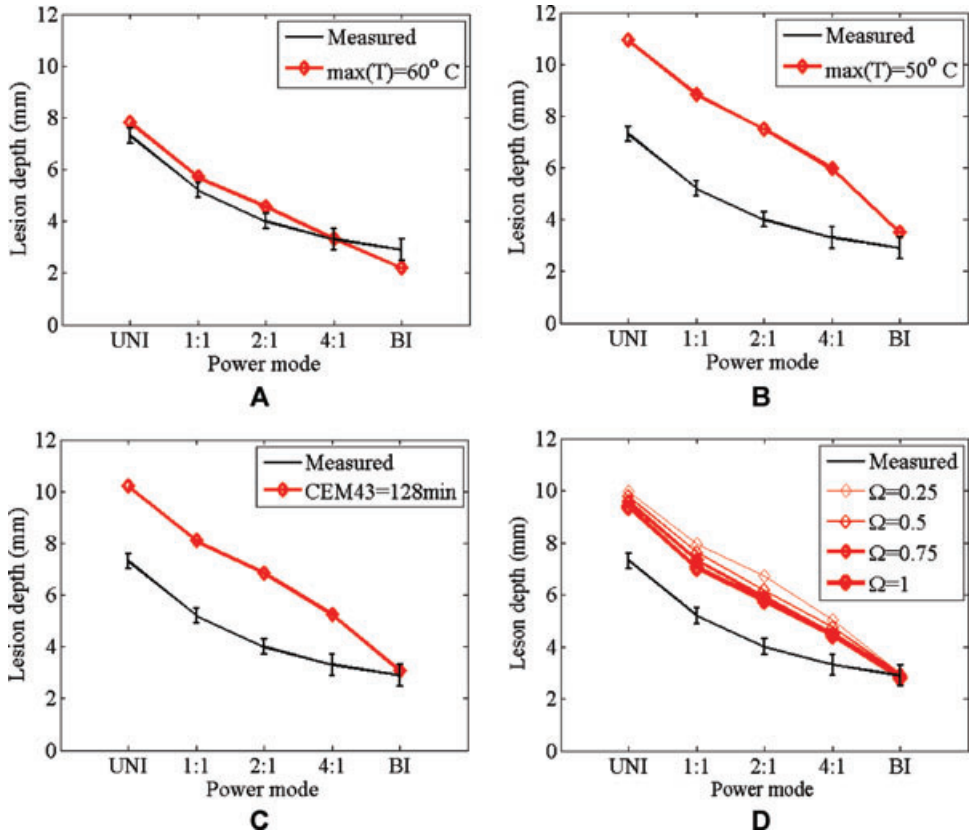

Figure 5. *Comparison of the in vitro lesion measurements with computational results: (A) maximum tissue temperature ≥60°C, (B) maximum tissue temperature ≥50°C, (C) cumulative equivalent minutes at 43°C (CEM43), and (D) the Arrhenius chemical reaction rate relationship (Ω = 1 represents irreversible damage). Results are consistent with the hypothesis that lesion discoloration (as measured in vitro) is well matched by tissue temperature of 60°C whereas lesion depth according to tissue viability is well matched by tissue temperature of 50°C.*

et al. demonstrated that the creation of contiguous lesions is challenging for multielectrode catheters delivering unipolar RF current, but by phasing the RF current (delivering both unipolar and bipolar current simultaneously), long lesions of consistent depth can be created.[18] The lowest temperature isosurface in Figure 6 is at 50°C, which is clearly seen to extend to the symmetry planes, confirming the contiguity of the lesion. This observation can be made for all modes of power delivery. Our results show that lesions of significant depth were generated without approaching electrode–tissue interface temperatures of 100°C, which may lead to coagulum formation, steam pops, char, and/or an impedance rise, preventing efficient energy delivery.[19]

It has been suggested that specific complications associated with RF ablation, including esophageal fistula and PV stenosis, may be a result of energy titration and the extension of thermal damage.[20,21] Therefore, there is a need to control energy delivery to create transmural contiguous lesions without excessive power and depth, thereby limiting peripheral thermal damage to nontargeted tissues. Zheng et al. showed that phasing allows lesion depth and thermal injury to be varied significantly by changing the phase angle (effectively changing the ratio of bipolar/unipolar energy).[18] Our results show that as the proportion of unipolar energy increases, lesion depth increases, a trend predicted by the computational model and observed *in vitro*. These findings are consistent with *in vivo* data reported for this system by Wijffels et al.[22] Thus, with this system, the desired lesion depth might be selected by energy mode (unipolar, 1:1, 2:1, 4:1, or bipolar) according to anatomical location, potentially reducing peripheral damage in areas of sensitive anatomy.

In addition to being phased, the energy delivered by the ablation system we study is temperature-controlled and duty-cycled. In temperature-controlled ablation systems, power

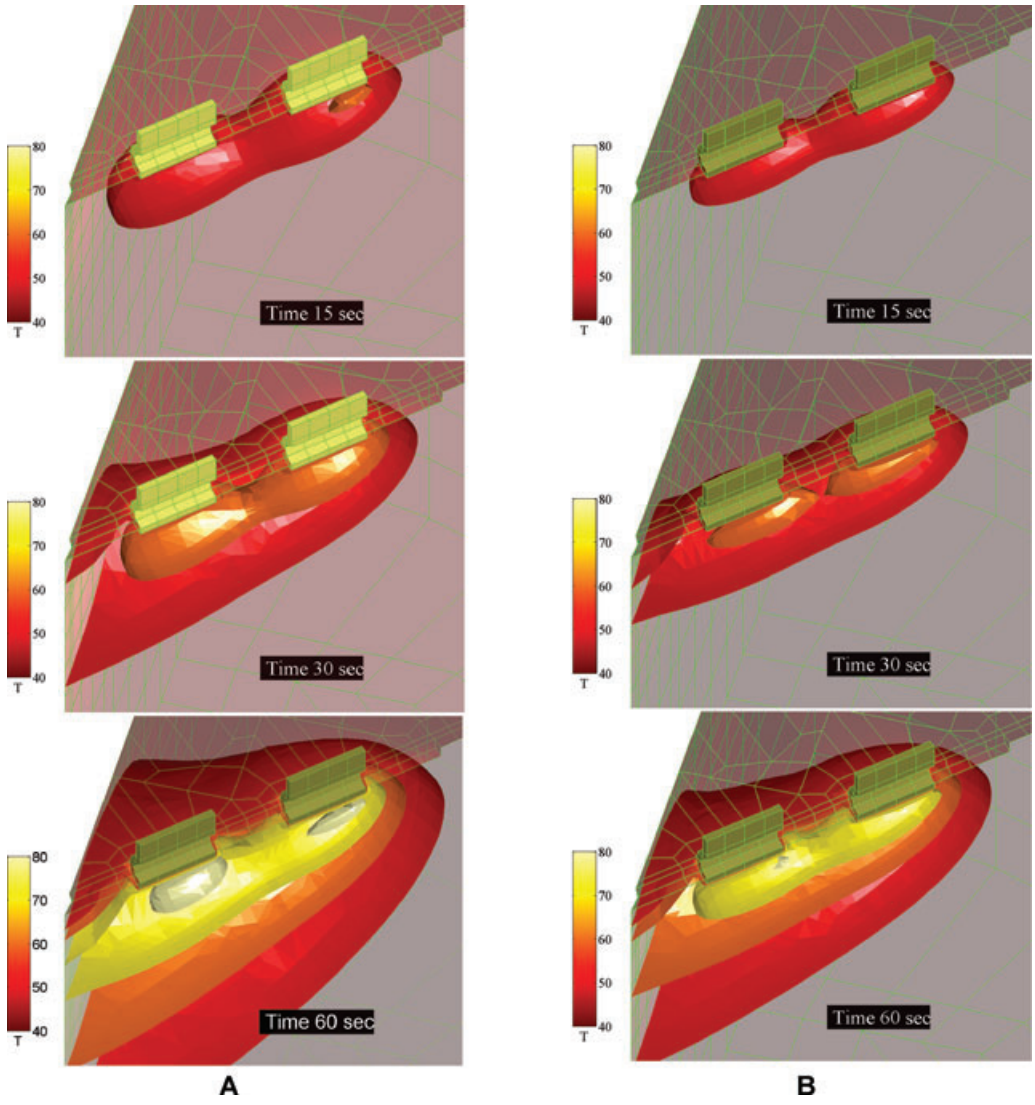

Figure 6. *Isosurfaces of temperature for the (A) 1:1 and (B) 4:1 (bipolar-to-unipolar) energy mode at 50, 60, 70, 80, 90°C at 15, 30, 60 seconds of heating. The higher ratio of bipolar to unipolar results in shallower lesions. Units of length, width, and depth as shown are millimeters.*

output is regulated to maintain the electrode–tissue interface temperature at a specified target temperature, typically between 60°C and 75°C.[23,24] Erdogan et al. demonstrated that to maximize the power output without overheating, RF energy can be duty-cycled, thereby allowing better electrode cooling and enabling more RF energy to be delivered, resulting in larger lesions than continuous RF energy.[25] Electrode design also has an effect on electrode cooling. To increase and optimize convective cooling, the electrodes of the MAAC catheter are designed with fins that protrude into the blood flow.

Our results show that MAAC device and GENius RF Generator are capable of creating contiguous lesions with a lesion depth that can be controlled by adjusting the ratio of bipolar to unipolar energy. Is it notable that the temperature distribution is relatively uniform and shows no signs of a significant edge effect, which has been observed with longer electrodes.[26] We hypothesize that the small electrode size allows the centrally located thermocouple to more effectively monitor the temperature across the entire electrode–tissue interface, suggesting an advantage of multiablation electrode catheters over single large ablation electrode catheters.

This validated model will allow for exploration of changing design parameters and clinical conditions expeditiously. Parameters of interest

for optimization include the duration of ablation, target temperature, electrode spacing, electrode size/shape/material, and catheter properties. Additional levels of sophistication to the model may further improve the correlation of results between the FEA simulation and *in vitro* experiments. Some areas of interest for future development may be modeling the temperature-dependent thermal material properties, a more sophisticated software controller incorporating the duty cycle, more accurate RF delivery for mixed modes (1:1, 2:1, 4:1), and the possibility of using a coupled fluid flow-thermal-electrical formulation.

Conclusions

A computational model for a unique multielectrode RF cardiac ablation system has been presented. The finite element model implements a novel solution for simultaneous bipolar and unipolar RF energy delivery, as well as incremental improvements (integrated software controller, and accuracy control in space and time) to previous modeling work. The model is validated with tissue temperature and lesion depth measurements from controlled *in vitro* ablations, and is found to be in close agreement with the experimental data. Both the *in vitro* and finite element model results demonstrate that lesion depth decreases as the bipolar-to-unipolar ratio increases, suggesting a potential clinical application to control lesion depth with higher fidelity than is currently available. The computational model can now allow the effect of various clinical conditions, which may be impractical to recreate on the bench-top, to be studied. In addition, the model can serve to provide support for proposed design improvements to the catheter and/or energy delivery.

Acknowledgments: The authors would like to acknowledge Sadaf Soleymani and Christine Pan for their work in establishing the foundation for the *in vitro* experimentation. The authors would also like to acknowledge Kathy Gao for her work in data collection and processing.

References

1. Zeppenfeld K, Stevenson W. Ablation of ventricular tachycardia in patients with structural heart disease. Pacing Clin Electrophysiol 2008; 31:358–374.
2. Nakagawa H, Jackman W. Catheter ablation of paroxysmal supraventricular tachycardia. Circulation 2007; 116:2465–2478.
3. Morady F. Radio-frequency ablation as treatment for cardiac arrhythmias. N Engl J Med 1999; 340:534–544.
4. Boersma L, Wijffels M, Oral H, Wever E, Morady F. Pulmonary vein isolation by duty-cycled bipolar and unipolar radiofrequency energy with a multielectrode ablation catheter. Heart Rhythm 2008; 5:1635–1642.
5. Berjano E. Theoretical modeling for radiofrequency ablation: State of the art and challenges for the future. Biomed Eng Online 2006; 5:24.
6. Cao H, Vorperian V, Tsai J, Tungjitkusolmun S, Woo E, Webster J. Temperature measurement within myocardium during in vitro RF catheter ablation. IEEE Trans Biomed Eng 2000; 47:1518–1524.
7. Plonsey R, Heppner D. Considerations of quasi-stationarity in electrophysiological systems. Bull Math Biophys 1967; 29:657–664.
8. Doss J. Calculation of electric-fields in conductive media. Med Phys 1982; 9:566–573.
9. Labonte S. A computer simulation of radio-frequency ablation of the endocardium. IEEE Trans Biomed Eng 1994; 41:883–890.
10. Jain M, Wolf P. A three-dimensional finite element model of radiofrequency ablation with blood flow and its experimental validation. Ann Biomed Eng 2000; 28:1075–1084.
11. Tangwongsan C, Will J, Webster J, Meredith K, Mahvi D. In vivo measurement of swine endocardial convective heat transfer coefficient. IEEE Trans Biomed Eng 2004; 51:1478–1486.
12. Krysl P. A Pragmatic Introduction to the Finite Element Method for Thermal and Stress Analysis: With the MATLAB Toolkit SOFEA. Hackensack, NJ, World Scientific Publishing Company, 2006.
13. Panescu D, Whayne J, Fleischman S, Mirotznik M, Swanson D, Webster J. Three-dimensional finite element analysis of current density and temperature distributions giving radio-frequency ablation. IEEE Trans Biomed Eng 1995; 42:879–890.
14. Nath S, Lynch III C, Whayne J, Haines D. Cellular electrophysiological effects of hyperthermia on isolated guinea pig papillary muscle: Implications for catheter ablation. Circulation 1993; 88:1826–1831.
15. Haemmerich D, Webster J, Mahvi D. Thermal dose versus isotherm as lesion boundary estimator for cardiac and hepatic radiofrequency ablation. Proceedings of the 25th Annual International Conference of the IEEE EMBS, Cancun, 2003, pp. 134–137.
16. Dewey W. Arrhenius relationships from the molecule and cell to the clinic. Int J Hyperthermia 1994; 10:457–483.
17. Labonté S. Numerical model for radio-frequency ablation of the endocardium and its experimental validation. IEEE Trans Biomed Eng 1994; 41:108–115.
18. Zheng X, Walcott G, Rollins D, Hall J, Smith W, Kay G, Ideker R. Comparison of the temperature profile and pathological effect at unipolar, bipolar and phased radiofrequency current configurations. J Interv Card Electrophysiol 2001; 5:401–410.
19. Haines D, Verow A. Observations on electrode-tissue interface temperature and effect on electrical impedance during radiofrequency ablation of ventricular myocardium. Circulation 1990; 82:1034–1038.
20. Martinek M, Bencsik G, Aichinger J, Hassanein S, Schefl R, Kuchinka P, Nesser H, et al. Esophageal damage during radiofrequency ablation of atrial fibrillation: Impact of energy settings, lesion sets, and esophageal visualization. J Cardiovasc Electrophysiol 2009; 20:726–733.
21. Ravenel J, McAdams H. Pulmonary venous infarction after radiofrequency ablation for atrial fibrillation. Am J Roentgenol 2002; 178:664–666.
22. Wijffels M, Oosterhout M, Boersma L, Werneth R, Kunis C, Hu B, Beekman J, et al. Characterization of in vitro and in vivo lesions made by a novel multichannel ablation generator and a circumlinear decapolar ablation catheter. J Cardiovasc Electrophysiol 2009.
23. Langberg J, Calkins H, el-Atassi R, Borganelli M, Leon A, Kalbfleisch S, Morady F. Temperature monitoring during radiofrequency catheter ablation of accessory pathways. Circulation 1992; 86:1469–1474.
24. Calkins H, Prystowsky E, Carlson M, Klein L, Saul J, Gillette P. Temperature monitoring during radiofrequency catheter ablation procedures using closed loop control: Atakr multicenter investigators group. Circulation 1994; 90:1279–1286.
25. Erdogan A, Carlsson J, Roederich H, Schulte B, Sperzel J, Berkowitsch A, Neuzner J, et al. Comparison of pulsed versus continuous radiofrequency energy delivery: Diameter of lesions induced with multipolar ablation catheter. Pacing Clin Electrophysiol 2000; 23:1852–1855.
26. McRury I, Panescu D, Mitchell M, Haines D. Nonuniform heating during radiofrequency catheter ablation with long electrodes. Circulation 1997; 96:4057–4064.

Appendix

The estimation of the convection heat transfer coefficient on the top surface of the specimen exposed to the saline bath is described here. An aluminum alloy block (44 × 31.5 × 15.5 mm; McMaster-Carr, Santa Fe Spring, CA, USA) was insulated with 12.5-mm-thick high-density polystyrene foam (McMaster-Carr, Santa Fe Spring, CA, USA) from five sides, leaving only the top surface opened to convective cooling. The T-thermocouples (Omega Engineering, Stamford, CT, USA) were used to measure the temperature of the aluminum block at three locations: the center of the aluminum block at depth of 3 mm, 7.5 mm, and 12 mm. The aluminum block was heated up to 120°C using a heat gun (Master Appliance Cop., Racine, WI, USA). The aluminum block was immediately placed in the polystyrene foam insulation box. The insulated aluminum alloy block was placed in a 37°C saline water bath and the flow rate was set to 1.8 L/min. The top foam insulation of the aluminum block was then removed to expose the top surface of the aluminum block to saline flow. The temperatures of the cooling aluminum block were recorded. (The flow system and the temperature recording system were described in detail in the Method section.) The experimental rig (the aluminum block plus the insulation) was modeled with a three-dimensional mesh, with prescribed temperature of 37°C on the outer surfaces of the insulation, and convection heat transfer from the aluminum block into the saline flow. The coefficient of the convection heat transfer was considered a free parameter, which was iteratively adjusted to yield an optimal fit of the computed temperatures to the experimental data (in the root mean square sense).